Rationalisation of the Micromechanisms Behind the High-Temperature Strength Limit in Single-Crystal Nickel-Based Superalloys

Daniel Barba, Ashton J. Egan, Yilun Gong, Michael J. Mills, and Roger C. Reed

Abstract

The peculiar atomic structure of γ' precipitates [Ni_3(Al/Ti)-$L1_2$] in Ni-based superalloys produces high-energy faults when dislocations glide them, giving their significant strength at high temperatures. The mechanisms behind the strength failure of these alloys above 700–800 °C are still controversial. Recent advances in atomic resolution microscopy have allowed to study these mechanisms with unprecedented detail. In our study, we have characterised in a careful systematic study a SX-[001] superalloy from RT to 1000 °C. Multiscale microscopy (TEM and SEM) has been combined with physical metallurgy and atomistic modelling to fully understand the correlation between the strength drop and the observed changes in the γ' shearing mechanism. Our results show that, far from previous beliefs, the initial failing of alloy strength is not a consequence of the activation of dislocation climbing. Instead, there is a transition between three different mechanisms: ($T < 750$ °C) continuous planar stacking faults below, ($T = 750$ °C) APB shearing at the strength peak anomaly and ($T > 800$ °C) extensive twin deformation after the yield drop. Local chemical changes around the γ' shearing dislocations boost these changes, thus producing the sudden drop of strength.

Introduction

Resistance to high-temperature plasticity is a significant advantage of the nickel-based superalloys, particularly when in single-crystal form. This important characteristic comes from a careful arrangement of shear resistant γ' precipitates. The high-energy faults formed when dislocations glide through these precipitates are known to provide this unique strength at high temperatures. This important mechanism becomes ineffective when the shearing dislocations have enough mobility to overcome the γ' precipitates at high temperature [6,32]. Historically, this was the consensus reason for the sudden drop of strength observed above 700 °C in these alloys. But is this the case?

In the recent years, advances in atomic resolution chemical microscopy (atom probe and TEM-EDX) have allowed the study of the population of mechanisms in this temperature regime with unprecedented detail [2,5,7,11,26,29] complementing previous studies on plasticity in Ni_3Al system [9,30,31]. These studies have shown the presence of other complex diffusion mechanisms different from the traditional dislocation climbing [2,7]: traditional dislocation shearing is aided by segregation processes leading to changes in the plastic strength above 700 °C.

However, there is a key-point missing: these studies are constrained to limited deformation regimes, thus not providing a complete picture of the mechanism. What is clearly needed to extract a convincing theory is a systematic study between the temperature, appearance of segregation

D. Barba (✉)
Universidad Politecnica de Madrid, Madrid, Spain
e-mail: daniel.barba@upm.es

A. J. Egan · M. J. Mills
Department of Materials Science and Engineering/Center for Electron Microscopy, The Ohio State University, Columbus, OH, USA
e-mail: egan.74@buckeyemail.osu.edu

M. J. Mills
e-mail: mills.108@osu.edu

Y. Gong
Department of Materials, University of Oxford, Oxford, UK
e-mail: yilun.gong@materials.ox.ac.uk

R. C. Reed
Department of Engineering Science, University of Oxford, Oxford, UK
e-mail: roger.reed@eng.ox.ac.uk

micromechanisms and loss of strength. This is a critical step to design improved grades of superalloys. In this work, we present a high-resolution characterisation study of the evolution of the micromechanisms and segregation processes as a function of the temperature, and we will associate the transition between the different deformation mechanisms with the loss of strength in the alloy. The study is structured as follows: first, a commercial SX-superalloy is mechanically tested at seven different temperature conditions (from RT to 900 °C). Second, critical samples before, at, and after the yield drop are selected for advanced TEM-EDX analysis. Third, the microsegregation levels and their chemical species associated with the dislocation shearing are quantified for each temperature. Finally, this observed behaviour is rationalised and modelled using density functional theory (DFT), and the observed yielding behaviour is extracted from the different micromechanism transitions.

Methods

Material and Experimental Methods

The single-crystal superalloy MD2 of composition Ni-11.2Al-9.3Co-5.3Cr-2.6W-2Ta-1.65Ti-1.33Mo-0.2Si-0.03Hf (at.%) is used in this study. The material was solution treated at 1275 °C for 8 h, followed by ageing for 6 h at 1080 °C, and finally at 870 °C for 16 h. The orientation of the bulk crystal was checked using backscattered electron diffraction (EBSD) analysis prior to extracting creep samples. A deviation from the ideal nominal orientation is $\langle 001 \rangle$ with less than 5° error.

Compression experiments under a constant displacement rate of the cross-head producing an initial strain rate of $\dot{\varepsilon} = 10^{-5}s^{-1}$ were performed at different temperatures covering the strength drop regime of the alloy (testing temperatures = 20, 400, 650, 750, 800, 850, and 900 °C). Cylinders of 5 mm diameter and 5 mm height were employed for the compression tests in an Instron servo-electric machine. In addition to the cross-head displacement, digital image correlation (DIC) was used to track the sample deformation for all tests. The tests were stopped for all specimens when 5% of total DIC strain was reached. Once the test was stopped, the furnace was open and displaced on rails away from the loading frame leaving the sample cooling down in the air. Loading on the sample was kept until a temperature of 200 °C was reached.

Post-mortem examination prior to scanning transmission electron microscopy (STEM) analysis was carried out in order to identify the deformation mechanisms after plastic deformation. One of the axial facets of the samples were grinder and polished finished with colloidal silica in order to identify the $\langle 001 \rangle$ crystal poles of the sample perpendicular to the compression orientation. Once identified, the cylinders were cut along one of the $\langle 001 \rangle$ planes perpendicular to the compression direction in order to extract STEM foils normal to $\langle 011 \rangle$ orientation using an FEI Helios NanoLab Dual-Beam 600 focused ion beam (FIB). This assures that planar faults are viewed edge-on using high-angle annular dark field (HAADF) zone axis imaging. Samples were thinned at 5 kV and then further cleaned using a Fischione NanoMill. Energy-dispersive X-ray analysis (EDX) of the foils was performed on an image-corrected Titan3™ 60–300 kV with a Super-X detector utilising the Bruker ESPRIT software. Integrated line scans were conducted and quantified through Cliff–Lorimer analysis [10] using experimental K_α energies for Ni, Co, Al, Cr, and Ti. L_α was used for the case of Mo. The Cu specimen holder signal was avoided by using the M_α lines for Ta and W since the L_α Ta and W peaks corresponded too closely to a Cu peak to be accurately considered. Deconvolution for the W and Ta M_α peaks, as well as background subtraction, was used to reduce the influence of bremsstrahlung. For EDS line scan analysis, to reduce the noise and smooth the data, small amounts of averaging were used. Using this setup, the noise can be reduced and no large effects on the variation of composition along the line scans were observed. Detrimental artefacts from foil thickness to the EDS spectrum like beam spreading or low EDS counts were mitigated by controlling the specimens thickness during the thinning process on the FIB. The FIB foil was thinned to around an estimated 20–50 nm where both foil thickness effects are observed to be avoided. Higher atomic resolution STEM analysis was performed using a probe-corrected Titan3™ 60–300 kV.

DFT Calculations

Density functional theory (DFT) calculations were performed to rationalise the experimental results through the calculation of antiphase boundary (APB) fault energies γ. The change in fault energy produced by segregation to the fault is expressed as:

$$\Delta\gamma = \frac{(E_{\text{fault}}^{\text{segregated}} - E_{\text{perfect}}^{\text{segregated}}) - (E_{\text{fault}}^{\text{Ni}_3\text{Al}} - E_{\text{perfect}}^{\text{Ni}_3\text{Al}})}{A} \tag{1}$$

where $E_{\text{fault}}^{\text{segregated}}$, $E_{\text{perfect}}^{\text{segregated}}$, $E_{\text{fault}}^{\text{Ni}_3\text{Al}}$, and $E_{\text{perfect}}^{\text{Ni}_3\text{Al}}$ are the energies of a segregated APB cell, a perfect segregated cell, a Ni–Al APB cell, and a Ni–Al perfect cell, respectively. These energy terms are extracted from Ni$_3$Al supercell calculations consisting on 12-{111} layers with 16 atoms on each layer, with a perfect stacking sequence or introducing and APB defect in the cell. To quantify the segregation effect on the stacking fault energy, Co, Cr, and Mo atoms were introduced in the Ni1 sites at the APB plane [21]. All calculations were performed using the projector augmented-wave (PAW) method [3] as implemented in the Vienna ab initio simulation

package (VASP) [13,14] with the provided PAW potentials [15]. The generalised gradient approximation (GGA) with Perdew–Burke–Ernzerhof (PBE) [20] parametrisation was utilised for the exchange-correlation functional. A $3\times3\times1$ Monkhorst–Pack k-point mesh [19] was used to sample the Brillouin zone in all calculations with a cut-off energy of 350 eV. Ions were fully relaxed with a force criterion of 5×10^{-3} eV/Å. Spin polarisation was included in all calculations with initial magnetic moments set as 1.5 μ_B for Co, 0.6 μ_B for Cr, 0.8 μ_B for Ni, and zero for Mo & Al.

Results

In this section, the mechanical and experimental results extracted from MD2 alloy will be presented. First, the mechanical response of the alloy is analysed, and the selection of temperature conditions for TEM samples is motivated. Then, the mechanisms operating at each of the mechanical regimes are elucidated using STEM atomic resolution microscopy. Although a large number of STEM images of each temperature conditions have been studied, a reduced set of representative ones is presented in this work. Finally, the local chemical changes associated with each of the faults are studied using TEM-EDX technique.

Mechanical Results

The mechanical behaviour for the different testing conditions is presented in Fig. 1a. Due to the high nonlinearity of the elastic regime in the curves, the yield stress Fig. 1b is calculated by translating by 0.2% deformation a straight line with an approximate slope equal to the linear elastic regime of each curve and identifying the intersection with the stress–strain curve. It can be observed a reduction of the hardening levels as the temperature increases and a sudden drop of properties after 750 °C. The strength of the alloy present a flat region up to 650 °C with a slight increase at 750 °C and finally a sudden drop for $T > 750°$. This behaviour has been previously observed in other SX-superalloys [22,23]. In order to rationalise micro-mechanically the anomalous yielding behaviour between 650–750 °C and the subsequent yield drop specific samples between 650 and 850 °C were selected for atomic resolution TEM-EDX microstructural and chemical analysis of their deformation structures. The selected conditions are: (1) 650 °C before the yield drop, (2) 750 °C just as the yield drop, and (3) 800 °C and (4) 850 °C after the yield drop.

Deformation Mechanisms Analysis

The deformation structures of the selected samples are presented next. STEM images of the 650 °C sample are presented in Fig. 2 corresponding to the temperature region below yield anomaly. The image shows a high density of continuous faults preferentially along one slip direction, with a reduced number of them along a second slip system (Fig. 2b). These deformation structures are in agreement with other studies performed on the same alloy under creep conditions [1,2]. These faults extend both in γ' and γ phases, with dislocation pile-ups formed in the latter phase. More detailed analysis presented later confirms a population of SESFs between these faults, with a minority evolving to a microtwin stage.

An example of STEM images of the 750 °C sample is presented in Fig. 3, corresponding to the peak of anomalous yield.
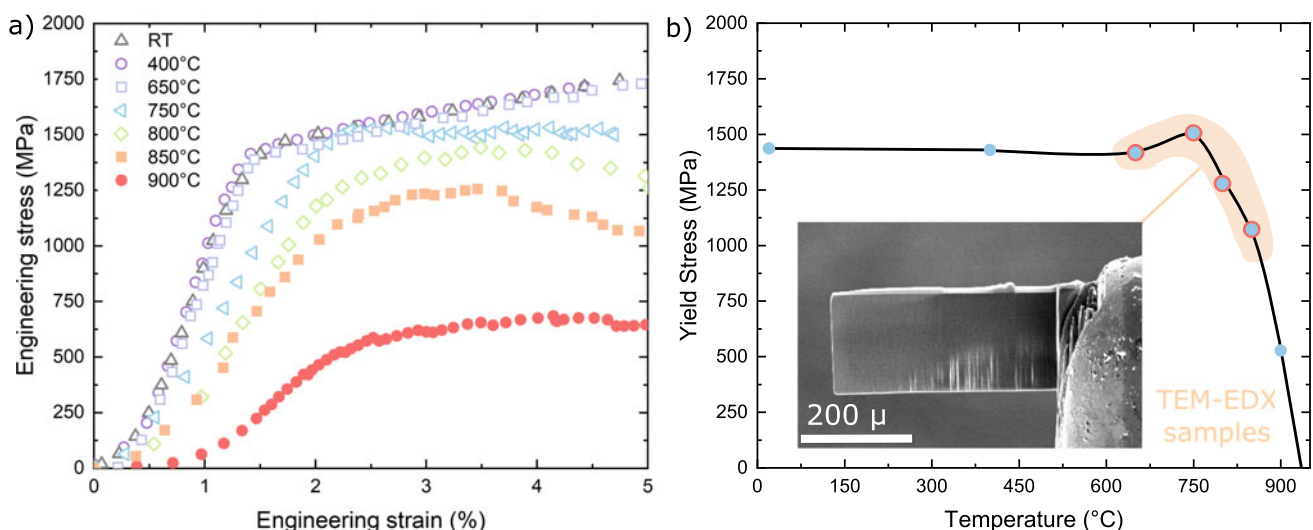
Fig. 1 **a** Mechanical stress–strain curve of MD2 superalloy for the different testing conditions experimented in this study. **b** Yield stress of MD2 alloy under compression at $\dot{\varepsilon} = 10^{-5}\mathrm{s}^{-1}$ as a function of temperature and detail of the testing conditions at which TEM samples are extracted
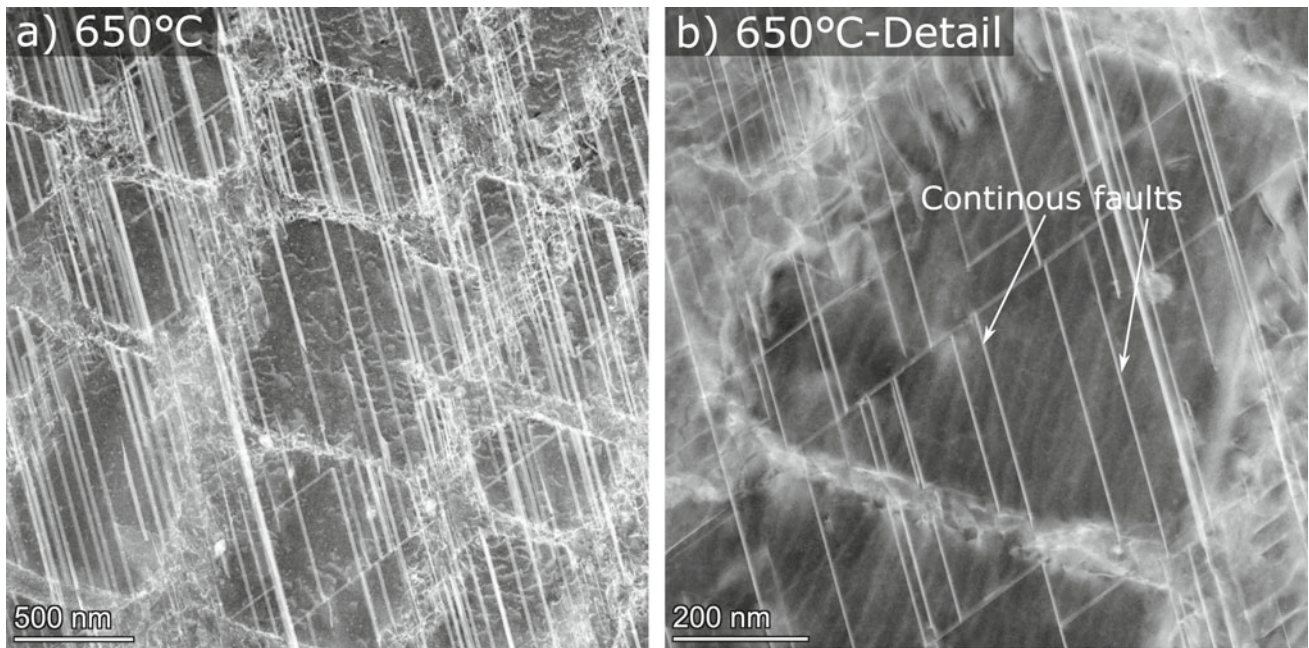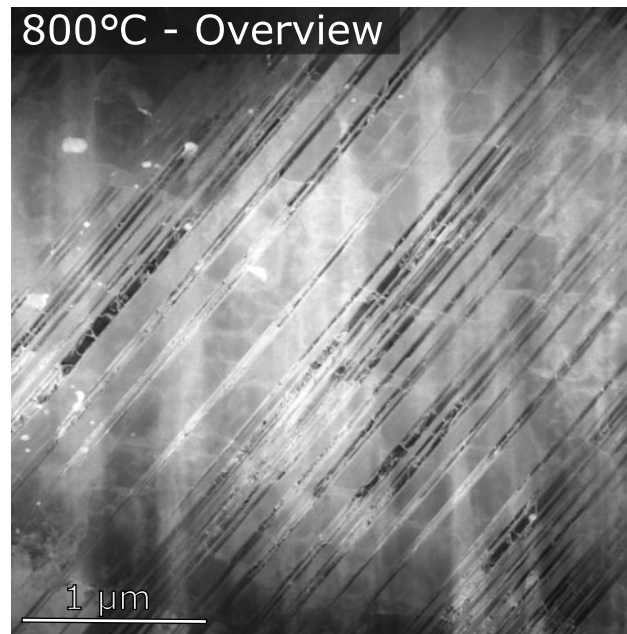
Fig. 2 STEM micrograph of the deformation structures observed at 650 °C, overview (**a**) and detail (**b**). A high density of continuous planar faults is observed along the whole sample
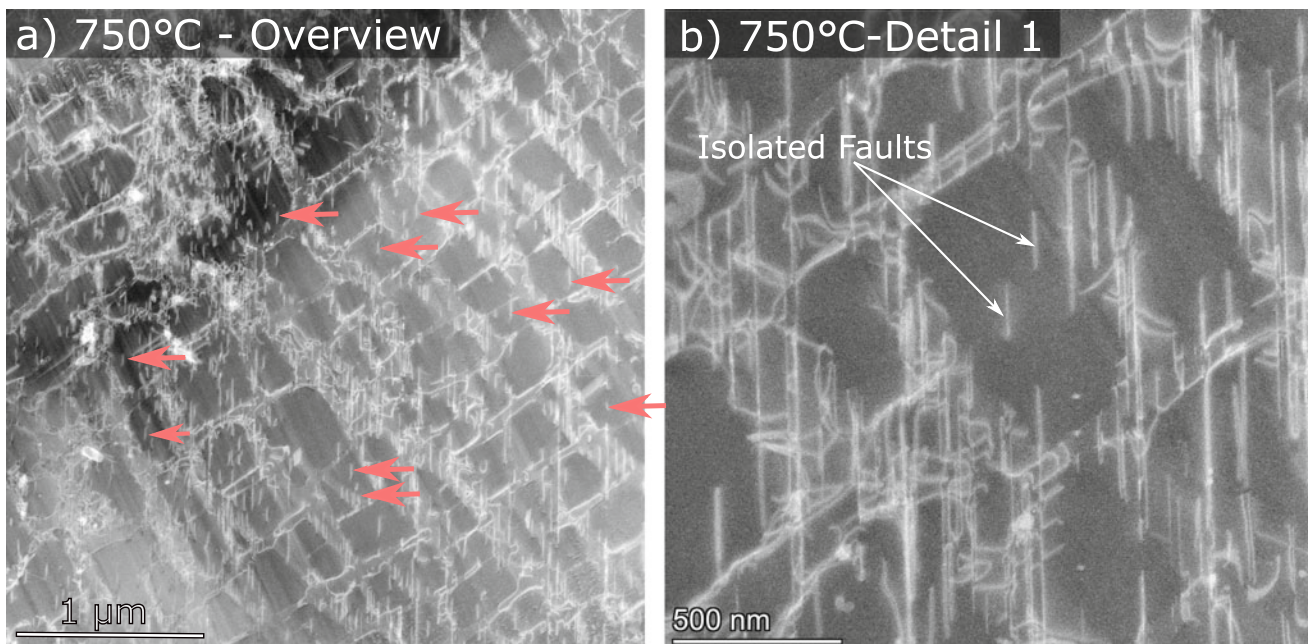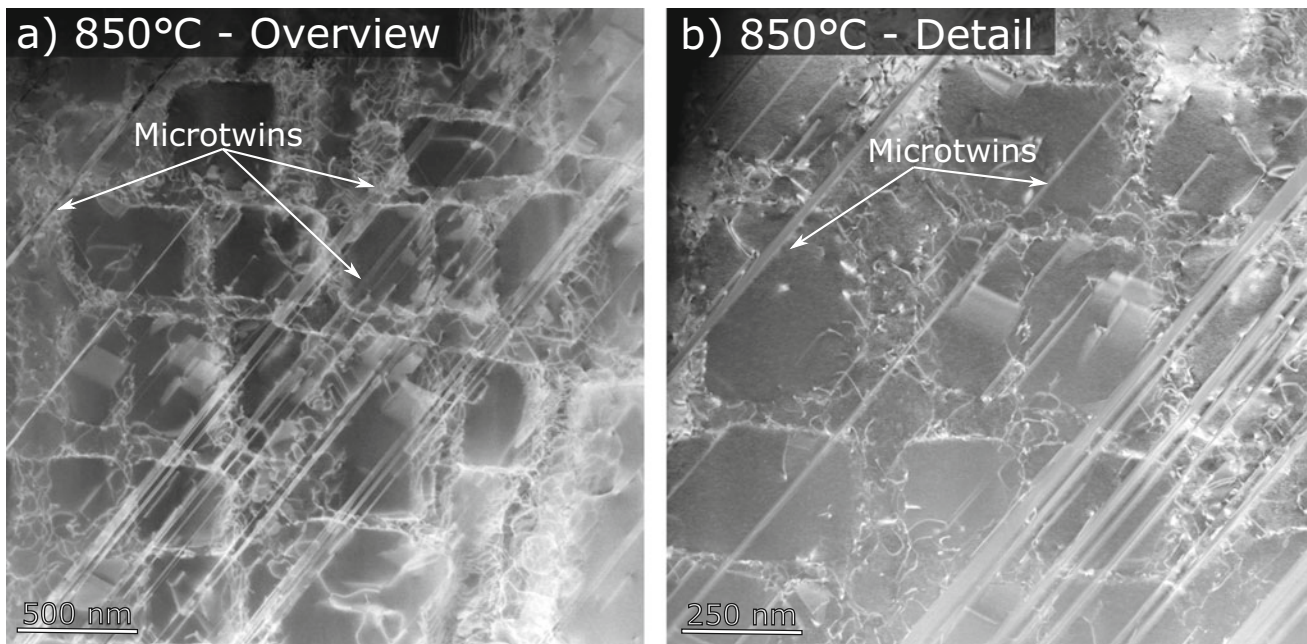

Fig. 3 STEM micrograph of the deformation structures observed at 750 °C, overview (**a**) and detail (**b**). Dissociated dislocation faults (later confirmed as APBs) populate the whole TEM sample

The deformation structures are completely different from the ones observed at 650 °C. Most of the faults are now formed by dissociated dislocations, presenting short extensions. Only a small number of extensive continuous faults have been spotted in the foil. This indicates a change of deformation mechanism from single leading dislocations on each plane to a sys-

tem of leading and trailing dislocations with a fault between them (partials for the case of extrinsic and intrinsic faults and full dislocations for antiphase boundaries-APBs). This will be explained with further detail in the discussion section. Atomic-level resolution analysis on some of these faults has confirmed their APB structure with enhance contrast due to

Fig. 4 STEM micrograph of the deformation structures observed at 800 °C. High density of extensive microtwinning along γ and γ' phases is observed

Fig. 5 STEM micrograph of the deformation structures observed at 850 °C, overview (**a**) and detail (**b**). As in for 800 °C, a high density of microtwins is observed extending along both γ and γ' phases

elemental segregation (more details in the chemical analysis section).

Finally, STEM images of the deformation structures corresponding to the yield drop region at 800 °C and 850 °C are presented in Figs. 4 and 5. The predominant deformation mechanism here is microtwinning. Extensive continuous bands run all along the TEM studied regions following the preferential slip system. These bands have been identified as microtwins using atomic resolution TEM as microtwins (see the following section). The thickness of these microtwin bands varies from tens of atomic planes to nanometres, usually organised in bundles. This clearly indicates a change of deformation mechanism from APBs to extensive microtwins along the whole sample, presumably producing the sudden

drop of strength observed mechanically in Fig. 1 as indicated in the discussion section.

As a summary, there is a transition between (1) a predominance of **continuous faults** below the yielding anomalous temperature ($T < 750$ °C), to **APB shearing** at the anomalous peak temperature ($T = 750$ °C), and finally the predominance of extensive **microtwinning** at the yield drop ($T > 750$ °C). Chemical analysis of the fault types observed at different temperatures is presented next.

Detailed Analysis of Fault Structures

In this section, representative examples of the faults observed for each temperature will be used for TEM-EDX chemical analysis. For the case of 650 °C, a double-fault structure is analysed as presented in Fig. 6. Atomic order analysis of the faults confirms their extrinsic nature (Fig. 6a). The faults can be either complex faults (CESFs) or regular faults (SESFs) as the present analysis cannot distinguish between them. The faults present higher contrast in HAADF analysis indicating local changes in composition. EDX analysis confirms this. EDX maps are presented in Fig. 6b, c showing a strong segregation of Cr to the faults and less pronounced for the case of Co. These maps have been integrated parallel to the fault to show the concentration profiles perpendicularly to the faults as indicated in Fig. 6d, e. The concentration profiles confirm the segregation of Cr ($\approx +1$ at.%) and Co ($\approx +0.5$ at.%). These increases are compensated by the depletion of Al (-1 at.%) at the fault. No significant fluctuations were found in the other elements analysed (Ni, Mo, Nb, Ti, Ta, W). The segregation/depletion of these elements is in accordance with previous works on the same alloy [2] and other alloy systems [11,16,25,28], but all of them under creep loading conditions. Furthermore, recent modelling work of Mianroodi et al. [17] rationalises the segregation of Co and Cr to complex faults in γ' in Ni–Al–Co ternary system.

The chemical analysis for a representative fault observed at 750 °C is presented in Fig. 7. A fault terminating inside a γ' precipitate is selected as indicated in see Fig. 7a. Atomic analysis of the STEM image in Fig. 7a shows no planar sequence disorder along the fault, vanishing the possibility of being an extrinsic or intrinsic fault. Therefore, this fault is presumably an APB. The enhanced contrast at the fault indicates again changes in the local composition. EDX maps of the faults confirm this, with Cr and Mo segregating slightly to the fault. A slight depletion of Ni is also observed. No significant changes are observed for the other elements. This elemental segregation is less pronounced and differs from the observed in the case of the SESFs at 650 °C (Co is not segregated here, while Mo is segregated and instead of Al, Ni is depleted). On top of that, the segregation levels of Cr are considerably lower ($+\approx 0.3$ at.% Cr) than for the 650 °C case.

Finally, the extensive microtwins observed at 800 °C and 850 °C are studied in detail in Figs. 8 and 9, respectively. The microtwin boundaries appears to be segregated of Cr in both cases ($\approx +0.4$ at.% Cr) and of Co for the case of the microtwin at 800 °C ($\approx +0.2$ at.% Co). Depletion of Al at the twin boundaries is also observed (≈ -0.3 at.% Al). The concentration of all elements inside the twin recovers the γ' composition. This is in accordance with other microtwin observation in the literature [2,7,12,27,28].

As a summary, all the different types of faults observed for the four temperatures present a similar segregation phenomenon. Variations in their quantity and type of elements are identified between continuous faults/microtwins and APB. The connection between these segregation events, the different deformation mechanisms, and the observed mechanical performance are discussed in more detail in the following section.

Discussion and Rationalisation of the Observed Deformation Mechanisms

In this section, each of the three different deformation mechanisms observed under mechanical compression of SX-MD2 alloy is discussed in detail. Then, the relationship between the different mechanisms, segregation phenomenon, and observed mechanical behaviour is rationalised.

The transition between the three different governing mechanisms along with the connection to mechanical strength of the alloy is summarised in Fig. 10. The three different deformation mechanisms present different dislocation structures and physical processes:

- **$T<750$ °C - Continuous faults:** The mechanism governing at temperatures below the anomalous yield peak is the formation of continuous 1–2 layer stacking faults (extrinsic or intrinsic). The reaction of unlike a/2 ⟨110⟩ dislocations, and entry of leading partial configurations, is the more recently accepted explanation [2,23,25]. The continuous extension of the fault implies the presence of a locked dislocation at the trailing end. The observed strong segregation of Co and Cr to the faults suggests the presence of complex extrinsic and intrinsic faults, as the driving force for standard stacking faults of the observed elements (Cr, Co) is small compared with the complex faults [21]. This point was also stated in previous studies, but no absolute judgement can be stated in this sense based on the used experimental techniques [1,28].

- **$T = 750$ °C - APBs or dissociated dislocations faults:** At the anomalous yielding region, continuous faults are replaced by APB shearing. These occupy most of the precipitates observed. The segregation elements change slightly when compared to continuous faults: Co segrega-
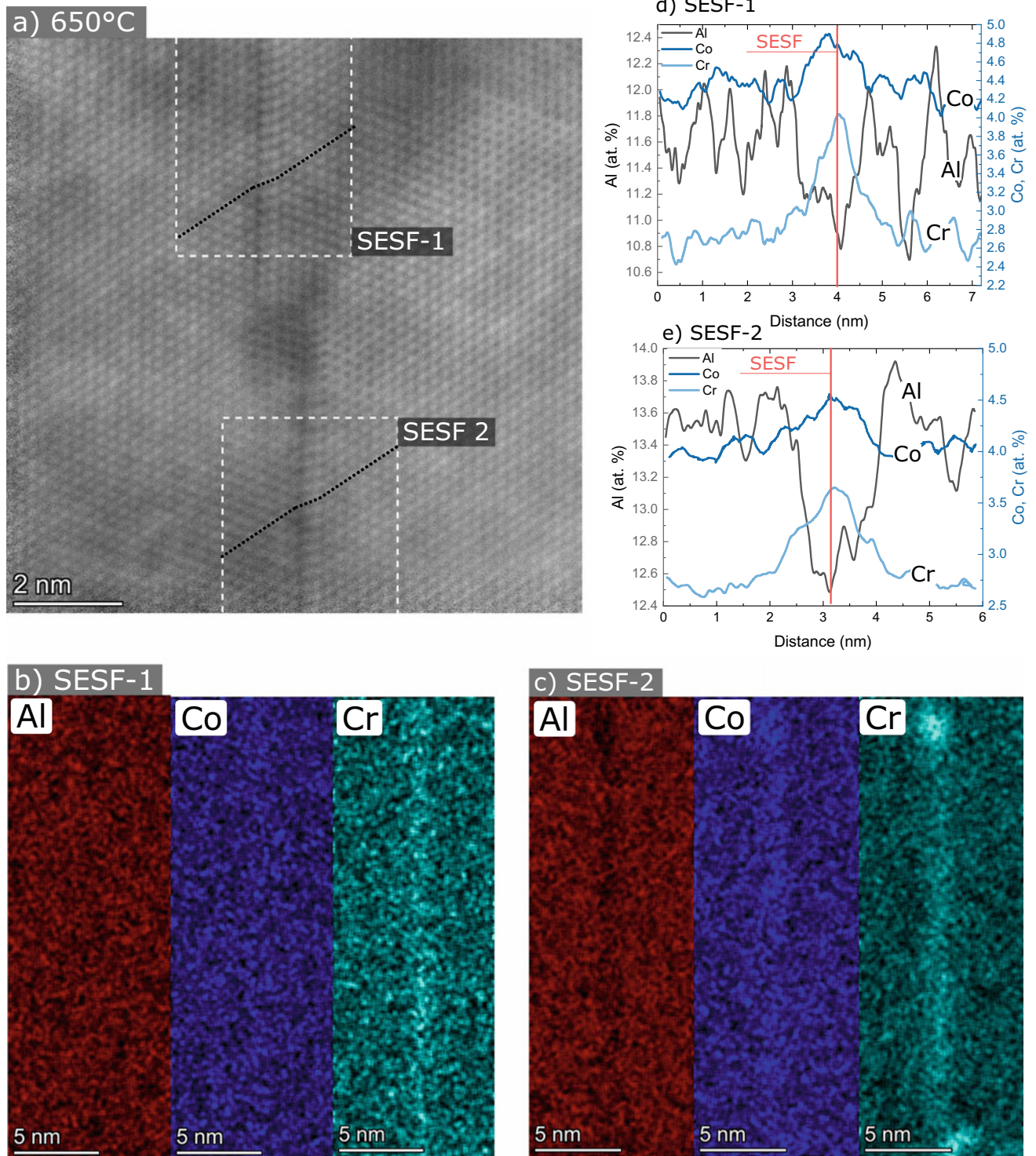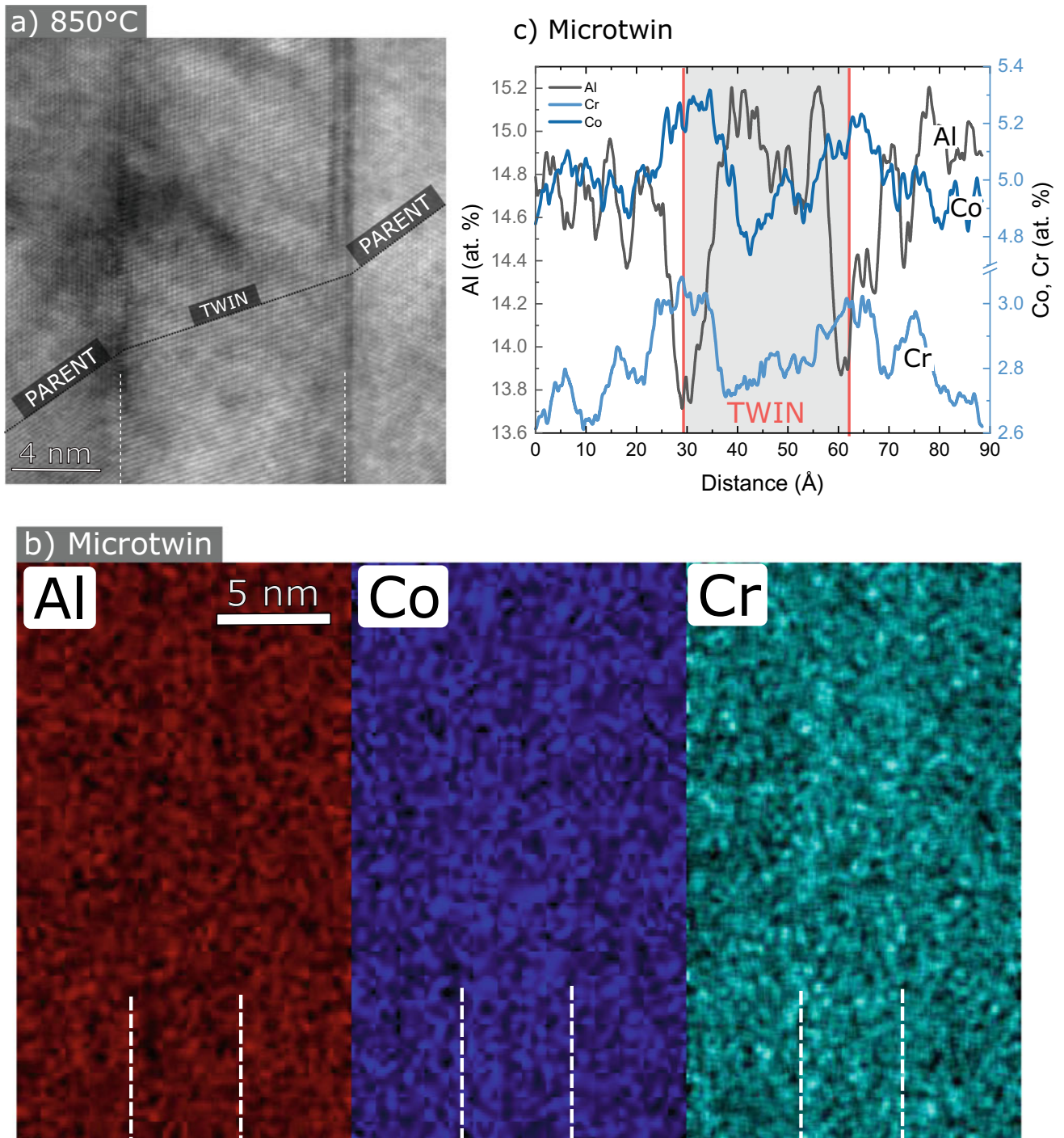
Fig. 6 STEM-EDX analysis of a representative fault formed during compression at 650 °C. **a** STEM micrograph of the faults structure (x2 SESF); **b**, **c** corresponding EDX elemental maps for the top and bottom SESFs, and **d**, **e** corresponding integrated EDX line scans showing the concentration profiles across both faults. The position of the faults is indicated by red lines in the concentration profiles
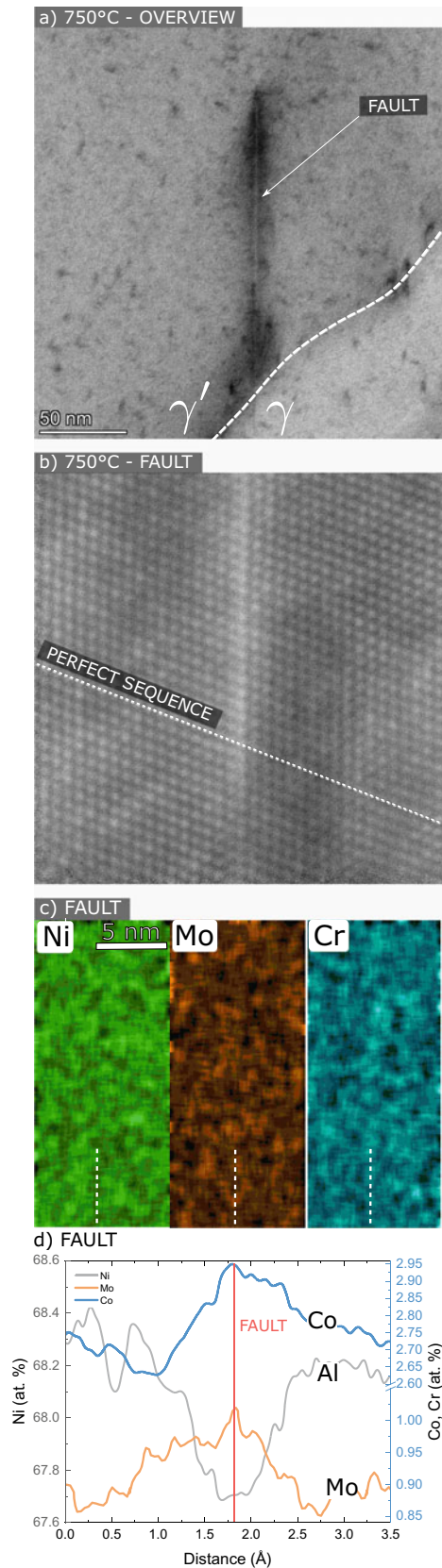
Fig. 7 STEM-EDX analysis of a representative fault formed during compression at 750 °C. **a** Overview STEM micrograph of the terminating fault structure (presumably APB) and detail of the fault showing a perfect stacking sequence at the fault; **b** corresponding EDX elemental maps for fault, and **c** corresponding integrated EDX line scans showing the concentration profiles across the fault. The position of the fault is indicated by red lines in the concentration profiles

Fig. 8 STEM-EDX analysis of a microtwin formed during compression at 800 °C. **a** STEM micrograph of the microtwin showing the reorientation of the lattice; **b** corresponding EDX elemental maps for the microtwin region with the twin boundaries indicated as white lines and **c** corresponding integrated EDX line scans showing the concentration profiles across the microtwin. The position of the microtwin boundaries is indicated by red lines in the concentration profiles
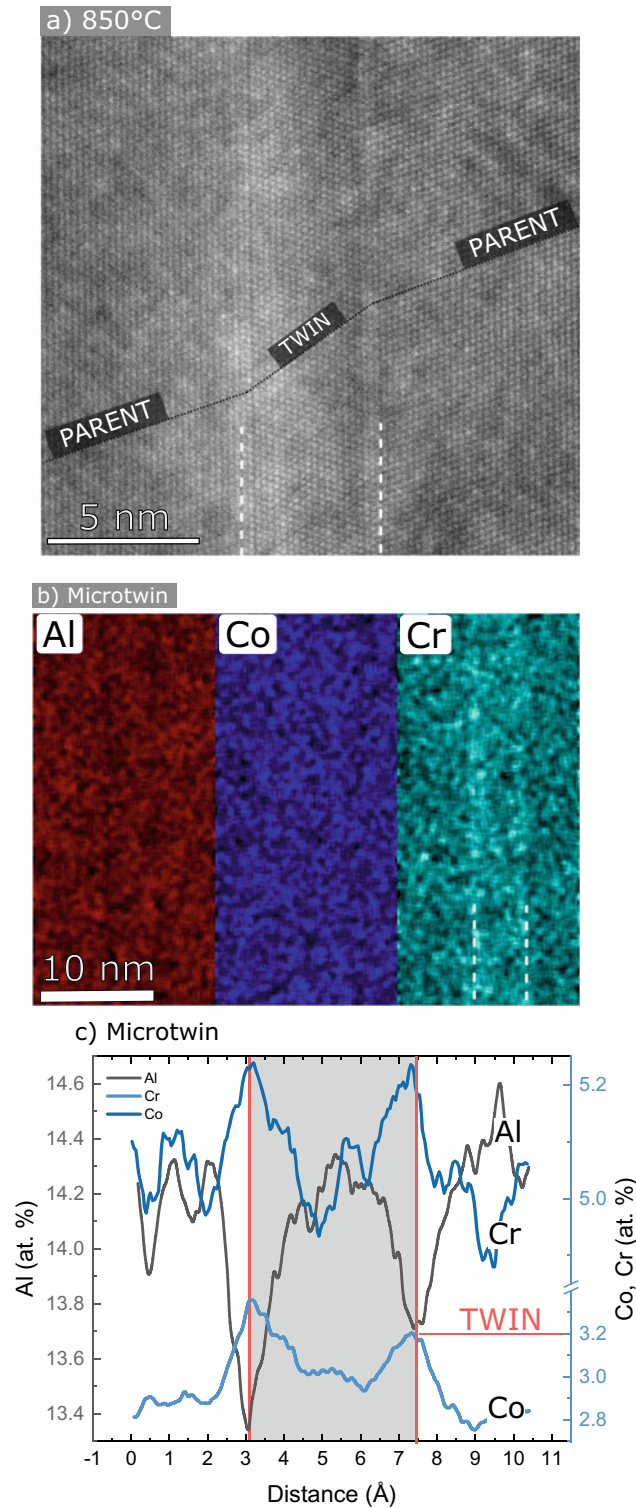
Fig. 9 STEM-EDX analysis of a microtwin formed during compression at 850 °C. **a** STEM micrograph of the microtwin showing the reorientation of the lattice, **b** corresponding EDX elemental maps for the microtwin region with the twin boundaries indicated as white lines, and **c** corresponding integrated EDX line scans showing the concentration profiles across the microtwin. The position of the microtwin boundaries is indicated by red lines in the concentration profiles
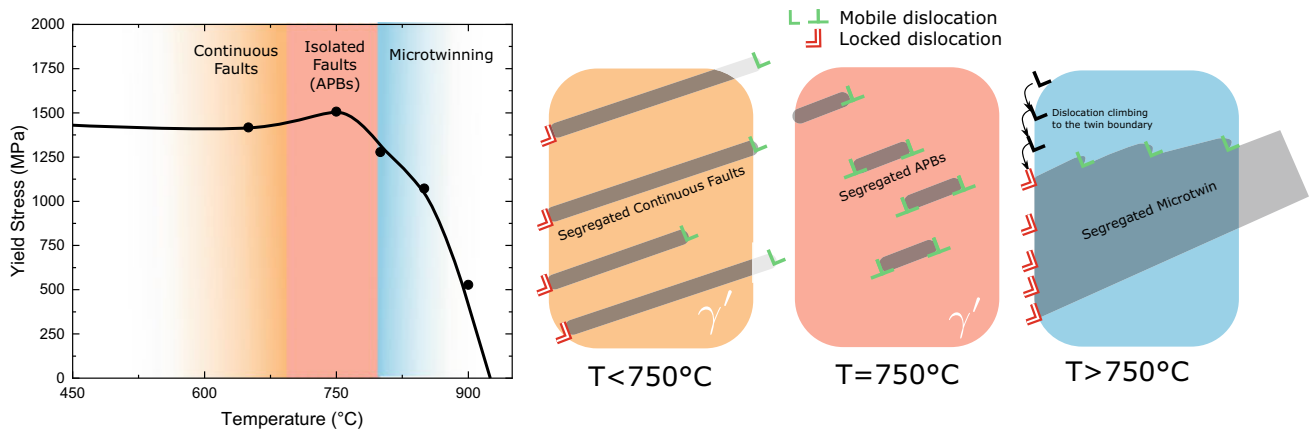
Fig. 10 Different operating deformation mechanism identified in Ni-based superalloy MD2 under compression at $\dot{\varepsilon} = 10^{-5}\,\mathrm{s}^{-1}$ as function of the temperature

tion is not observed while Mo segregation appears. These types of faults are produced by a set of two mobile full $\langle 110 \rangle$ dislocations, with the leading dislocation creating an APB and the trailing one restoring it.

- **T>750 °C - Microtwinning:** Finally, at higher temperatures, APB dissociated dislocations reduce their presence and a high density of microtwin bands appears. These types of faults are formed by continuous pass of $\langle 112 \rangle$ partial dislocation on adjacent {111} planes leaving a population of blocked trailing dislocations at the γ-γ' interface [1,28]. The segregation profiles are again similar to the continuous faults. However, the segregation is just confined at the twin boundaries, leaving the core of the twin unsegregated. This has great implications on the mechanical performance as, once the first twin layer is created, no further segregation elements need to be diffused to the twin from the surrounding material.

From the observed deformation mechanism, chemical analysis, and temperature dependencies, it is clear that segregation and other time-dependent processes control the transition between different mechanisms and thus, the observed mechanical behaviour at high temperatures of superalloys. These are discussed next.

The transitions between different deformation mechanisms define the observed mechanical dependence on temperature. For the first transition from continuous faults to APB shearing, there is a change of segregated elements present at the fault (from Co to Mo segregation). In order to arise light on this change of segregated elements, DFT analysis on segregated APBs has been performed as shown in Fig. 11. All the atoms of Ni in Ni1 sites at the APB fault plane has been replaced by Co, Cr, and Mo as indicated in Fig. 11a. The calculated fault energies for the different segregated APBs are presented in Fig. 11b. These results show the powerful effect of Mo and Cr in reducing the

stacking fault energy and thus the stress required for the creation of the APB fault, especially Mo. Cr effect is in accordance with previous results from Rao et al. [21]. Thus, the transition to APBs might be triggered by the increased mobilities by the higher temperatures of these slow diffusion elements such as Mo [4,18] observed in the APB and not in the continuous stacking faults. However, once an APB segregated fault is created at the γ-γ' interface, the gliding of this fault is limited to the diffusion of the segregation cloud coupled with it. This increases the stress required during constant displacement rate tests. In the case of the second mechanism transition, the factor triggering the formation of thick microtwins at higher temperatures is the necessity of piling up dislocations on adjacent {111} gliding planes. This phenomenon is statistically unlikely to happen without climbing of the shearing dislocation. This should include necessarily climbing short distances from the interception of the dislocation at the γ-γ' interface. This short climbing process requires a high mobility of the dislocation segments only possible at higher temperatures [6,8] which might explain the appearance of thick microtwins only above 750 °C for this alloy. On the other hand, once the first layer of a microtwin formed, no additional segregation elements are needed as the initial segregated twin boundary just needs to advance to the adjacent {111} plane as the gliding partial dislocation advances [1,24]. This has strong implications on the rate limiting processes governing the dislocation motion, as diffusion distances reduce considerably, to just one atomic spacing. At constant strain rate tests, this produce a drop of the stress required for extending these twins and thus deforming the material. Based on these premises and experimental observations, we can infer that the yield drop observed in this alloy experimentally is produced by the transition from APB faults with high gliding stress to deformation microtwins with low stress required for their extension.
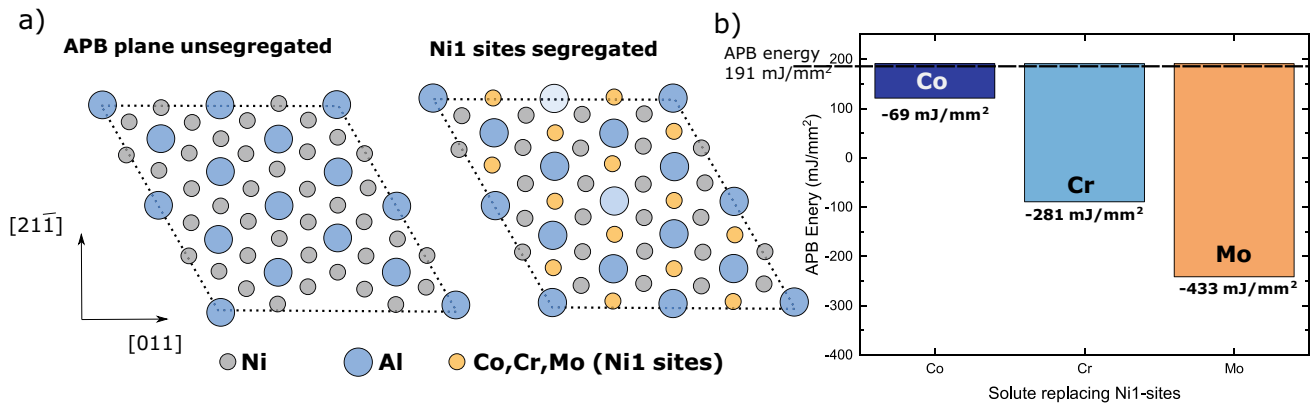
Fig. 11 **a** Atomic arrangements at the {111} APB plane of the unsegregated and segregated DFT supercells used in this study. All the Ni1 sites at the APB fault are substituted by segregate elements; **b** change is APB energy calculated from DFT when all Ni1 sites at the APB are substituted by the indicated elements

Conclusions

The relationship between deformation mechanisms and strength evolution with temperature of the SX-superalloy MD2 has been studied experimentally. The following conclusions arose from this study:

1. The yield strength response of the SX-MD2 alloy as a function of temperature can be split in three different regions: (1) flat strength region up to $\approx 750\,°C$, (2) anomalous yield peak at about $750\,°C$, and finally (3) a sudden strength drop about $\approx 750\,°C$.

2. Each of these three regions presents different deformation mechanisms elucidated by TEM analysis: (1) high density of 1–2 layer continuous faults extending to both γ and γ, (2) APB shearing within the γ' precipitates formed by coupled dislocations, (3) extensive microtwinning bands at the nm level extending to both γ and γ'.

3. All the faults studied show local segregation at their core (or twin boundaries for the case of the microtwinning). Region (1) and (3) faults (SESFs and microtwinning) are enriched with Cr and Co and depleted with Al. Faults at the yield strength peak (3) are enriched with Cr and Mo, while in this case there is a depletion of Ni at the fault.

4. Atomistic modelling of the segregation phenomenon to APB faults shows that the introduction of Cr and Mo atoms in the Ni1 sites of the fault reduces the energy abruptly, thus producing a positive driving force for the segregation of these elements and more importantly promotes the creation of APBs within the γ' precipitates. However, the gliding of these APBs through the γ' precipitates is restricted to the diffusion velocity of these elements.

5. The dislocation structures for the different observed mechanisms has been postulated. These have been used to rationalise the observed transition between deformation mechanism and the connected changes in the mechani-cal response of this alloy. The transition between different faults might be guided by the different levels and types of segregation types along with the necessity of partial dislocation climbing for microtwinning which is enhanced at higher temperatures.

References

1. Barba, D., Pedrazzini, D., Collins, A., Wilkinson, A., Moody, M., Bagot, P., Jérusalem, A., Reed, R.: On the microtwinning mechanism in a single crystal superalloy. Acta Materialia **127**, 37–40 (2017). https://doi.org/10.1016/j.scriptamat.2016.08.029. http://www.sciencedirect.com/science/article/pii/S1359646216304055

2. Barba, D., Smith, T., Miao, J., Mills, M., Reed, R.: Segregation-assisted plasticity in ni-based superalloys. Metallurgical and Materials Transactions A **49**(9), 4173–4185 (2018)

3. Blöchl, P.E.: Projector augmented-wave method. Phys. Rev. B **50**, 17953–17979 (1994). https://doi.org/10.1103/PhysRevB.50.17953

4. Chen, Y., Francis, E., Robson, J., Preuss, M., Haigh, S.: Compositional variations for small-scale gamma prime (γ') precipitates formed at different cooling rates in an advanced ni-based superalloy. Acta Materialia **85**, 199 – 206 (2015)

5. Eggeler, Y., Müller, J., Titus, M., Suzuki, A., Pollock, T., Spiecker, E.: Planar defect formation in the γ' phase during high temperature creep in single crystal coni-base superalloys. Acta Materialia **113**, 335–349 (2016). http://www.sciencedirect.com/science/article/pii/S1359645416302531

6. Epishin, A., Link, T.: Mechanisms of high-temperature creep of nickel-based superalloys under low applied stresses. Philosophical Magazine **84**(19), 1979–2000 (2004)

7. Freund, L., Messé, O.M., Barnard, J., Göken, M., Neumeier, S., Rae, C.: Segregation assisted microtwinning during creep of a polycrystalline L12-hardened Co-base superalloy. Acta Materialia **123**, 295–

304 (2017). https://doi.org/10.1016/j.actamat.2016.10.048. http://linkinghub.elsevier.com/retrieve/pii/S1359645416308151

8. Haghighat, S.H., Eggeler, G., Raabe, D.: Effect of climb on dislocation mechanisms and creep rates in γ'-strengthened ni base superalloy single crystals: A discrete dislocation dynamics study. Acta Materialia **61**(10), 3709 – 3723 (2013)

9. Hirsch, P.B.: A new theory of the anomalous yield stress in l1$_2$ alloys. Philosophical Magazine A **65**(3), 569–612 (1992). https://doi.org/10.1080/01418619208201539

10. Hoeft, H., Schwaab, P.: Investigations towards optimizing EDS analysis by the cliff-lorimer method in scanning transmission electron microscopy. X-Ray Spectrometry **17**(5), 201–208 (1988). https://doi.org/10.1002/xrs.1300170509

11. Kontis, P., Li, Z., Collins, D.M., Cormier, J., Raabe, D., Gault, B.: The effect of chromium and cobalt segregation at dislocations on nickel-based superalloys. Scripta Materialia **145**(Supplement C), 76 – 80 (2018). https://doi.org/10.1016/j.scriptamat.2017.10.005. http://www.sciencedirect.com/science/article/pii/S1359646217305912

12. Kovarik, L., Unocic, R., Li, J., Sarosi, P., Shen, C., Wang, Y., Mills, M.J.: Microtwinning and other shearing mechanisms at intermediate temperatures in Ni-based superalloys. Progress in Materials Science **54**, 839–873 (2009)

13. Kresse, G., Furthmüller, J.: Efficient iterative schemes for ab initio total-energy calculations using a plane-wave basis set. Phys. Rev. B **54**, 11169–11186 (1996). https://doi.org/10.1103/PhysRevB.54.11169

14. Kresse, G., Furthmüller, J.: Efficiency of ab-initio total energy calculations for metals and semiconductors using a plane-wave basis set. Computational Materials Science **6**(1), 15 – 50 (1996). https://doi.org/10.1016/0927-0256(96)00008-0. http://www.sciencedirect.com/science/article/pii/0927025696000080

15. Kresse, G., Joubert, D.: From ultrasoft pseudopotentials to the projector augmented-wave method. Phys. Rev. B **59**, 1758–1775 (1999). https://doi.org/10.1103/PhysRevB.59.1758

16. Makineni, S.K., Kumar, A., Lenz, M., Kontis, P., Meiners, T., Zenk, C., Zaefferer, S., Eggeler, G., Neumeier, S., Spiecker, E., Raabe, D., Gault, B.: On the diffusive phase transformation mechanism assisted by extended dislocations during creep of a single crystal conibased superalloy. Acta Materialia **155**, 362 – 371 (2018). https://doi.org/10.1016/j.actamat.2018.05.074. http://www.sciencedirect.com/science/article/pii/S1359645418304713

17. Mianroodi, J.R., Shanthraj, P., Kontis, P., Cormier, J., Gault, B., Svendsen, B., Raabe, D.: Atomistic phase field chemo-mechanical modeling of dislocation-solute-precipitate interaction in ni–al–co. Acta Materialia **175**, 250 – 261 (2019). https://doi.org/10.1016/j.actamat.2019.06.008. http://www.sciencedirect.com/science/article/pii/S1359645419303672

18. Minamino, Y., Yoshida, H., Jung, S.B., Hirao, K., Yamane, T.: Diffusion of platinum and molybdenum in Ni and Ni$_3$Al. In: Diffusion in Materials DIMAT 1996, *Defect and Diffusion Forum*, vol. 143, pp. 257–262. Trans Tech Publications Ltd (1997)

19. Monkhorst, H.J., Pack, J.D.: Special points for brillouin-zone integrations. Phys. Rev. B **13**, 5188–5192 (1976)

20. Perdew, J.P., Burke, K., Ernzerhof, M.: Generalized gradient approximation made simple. Phys. Rev. Lett. **77**, 3865–3868 (1996). https://doi.org/10.1103/PhysRevLett.77.3865

21. Rao, Y., Smith, T., Mills, M., Ghazisaeidi, M.: Segregation of alloying elements to planar faults in γ'-Ni$_3$Al. Acta Materialia **148**, 173–184 (2018)

22. Reed, R.: The Superalloys: Fundamentals and Applications. Cambridge (2006)

23. Reed, R., Rae, C.: 22 - Physical metallurgy of the nickel-based superalloys. In: D. Laughlin, K. Hono (eds.) Physical Metallurgy (Fifth Edition), pp. 2215–2290. Elsevier, Oxford (2014)

24. Smith, T.: Orientation and alloying effects on creep strength in ni-based superalloys. Ph.D. thesis, The Ohio State University (2016)

25. Smith, T., Esser, B., Antolin, N., Carlsson, A., Williams, R., Wessman, A., Hanlon, T., Fraser, H., Windl, W., McComb, D., Mills, M.: Phase transformation strengthening of high-temperature superalloys. Nature Communications **7**, 13434 (2016). https://doi.org/10.1038/ncomms13434 http://www.nature.com/articles/ncomms13434#supplementary-information

26. Smith, T., Esser, B., Antolin, N., Viswanathan, G., Hanlon, T., Wessman, A., Mourer, D., Windl, W., McComb, D., Mills, M.: Segregation and η phase formation along stacking faults during creep at intermediate temperatures in a Ni-based superalloy. Acta Materialia **100**, 19–31 (2015). https://doi.org/10.1016/j.actamat.2015.08.053. http://linkinghub.elsevier.com/retrieve/pii/S1359645415006308

27. Smith, T., Good, B., Gabb, T., Esser, B., Egan, A., Evans, L., McComb, D., Mills, M.: Effect of stacking fault segregation and local phase transformations on creep strength in ni-base superalloys. Acta Materialia **172**, 55 – 65 (2019). https://doi.org/10.1016/j.actamat.2019.04.038. http://www.sciencedirect.com/science/article/pii/S135964541930240X

28. Smith, T., Rao, Y., Wang, Y., Ghazisaeidi, M., Mills, M.: Diffusion Processes During Creep at Intermediate Temperatures in a Ni-based Superalloy. Acta Mater. **141**, 261–272 (2017). https://doi.org/10.1016/j.actamat.2017.09.027. http://www.sciencedirect.com/science/article/pii/S1359645417307607

29. Smith, T., Unocic, R., Deutchman, H., Mills, M.: Creep deformation mechanism mapping in nickel base disk superalloys. Materials at High Temperatures **33**(33), 1–12 (2016). https://doi.org/10.1080/09603409.2016.1180858

30. Suzuki, H.: Segregation of solute atoms to stacking faults. Journal of the Physical Society of Japan **17**(2), 322–325 (1962). https://doi.org/10.1143/JPSJ.17.322

31. Veyssiere, P., Douin, J., Beauchamp, P.: On the presence of super lattice intrinsic stacking faults in plastically deformed ni3al. Philosophical Magazine A **51**(3), 469–483 (1985). https://doi.org/10.1080/01418618508237567

32. Zhu, Z., Basoalto, H., Warnken, N., Reed, R.: A model for the creep deformation behaviour of nickel-based single crystal superalloys. Acta Materialia **60**(12), 4888–4900 (2012)